

# Gaussian Process-based Bayesian Quantum Characterization

Mohammad Motamed <sup>\*1,2</sup> and N. Anders Petersson <sup>†2</sup>

<sup>1</sup>Department of Mathematics and Statistics, University of New Mexico, Albuquerque, NM 87131

<sup>2</sup>Center for Applied Scientific Computing, Lawrence Livermore National Laboratory, Livermore, CA 94550

August 25, 2023

---

## Abstract

We present a Bayesian quantum characterization framework that takes into account uncertainties from both experimental data and the dynamical modeling of the experiment. We demonstrate that ignoring dynamical model uncertainty may lead to predictions that are inconsistent with the uncertainty present in quantum data. A Bayesian framework is proposed and applied to characterize a tantalum-based transmon device at Lawrence Livermore National Laboratory. We demonstrate how modeling uncertainty can be represented by a Gaussian process within the Bayesian framework, and how this approach improves the predictive capability of Lindblad's master equations applied to the Ramsey measurement protocol.

---

## 1 Introduction

Quantum characterization is the process of estimating quantum device parameters, such as transition frequencies and decoherence times. It is considered as an instrumental step in performing quantum (optimal) control, which is in turn essential for the implementation of robust quantum logical gates; see e.g., [1, 2]. Conventional approaches for determining device parameters involve deterministic curve fitting techniques and/or frequency domain analysis applied to a parametric Hamiltonian model that describes the dynamics of the quantum device; see e.g., [3, 4, 5]. These approaches, however, do not account for all uncertainties that are present in current Noisy Intermediate-Scale Quantum (NISQ) systems [6]. To address this shortcoming, various Bayesian quantum characterization and Hamiltonian learning approaches have been proposed; see e.g., [7, 8, 9, 10, 11, 12, 13, 14, 15]. Bayesian approaches aim at taking the uncertainty in quantum device parameters into account, thereby delivering posterior probability density distributions rather than deterministic numerical values for the parameters. Not only can such posteriors guide experimenters in their design of quantum devices, they can also be utilized to design more robust controls through the use of risk neutral optimization [16].

One important type of uncertainty in NISQ devices is experimental uncertainty. In the following we focus our discussion on superconducting transmon systems, residing inside a dilution refrigerator operating at milli Kelvin temperatures. For such devices, sources of experimental uncertainty include

---

\*motamed@unm.edu

†petersson1@llnl.gov

state preparation and measurement (SPAM) errors, fluctuations in the coupling between the quantum device and its environment, and the variability in gain of the quantum limited amplifiers that enable weak device signals to be amplified (by several orders of magnitude), such that they can be analyzed at room temperature. Figure 1 displays the measured populations as functions of dark time from Ramsey experiments on a tantalum-based transmon device [17], within the Quantum Device and Integration Testbed (QuDIT) at Lawrence Livermore National Laboratory; see more details in Section 5.1. Here, the

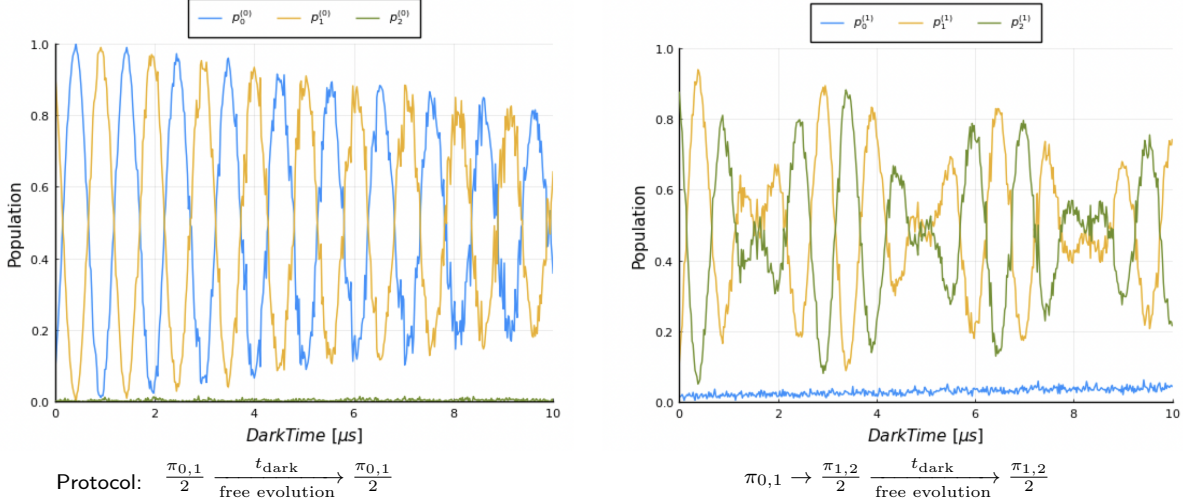


Figure 1: Populations as functions of dark time for Ramsey  $0 \leftrightarrow 1$  (left) and  $1 \leftrightarrow 2$  (right) experiments. In the protocols,  $\pi_{k,k+1}$  and  $\frac{\pi_{k,k+1}}{2}$  denote  $\pi$  and  $\frac{\pi}{2}$  pulses for the  $k \leftrightarrow k+1$  transition.

Ramsey measurements are distinctly corrupted by noise, and the noise has a complex structure. In the  $0 \leftrightarrow 1$  case, the noise increases as the dark time increases, and in the  $1 \leftrightarrow 2$  case, the noise increases largely in the phase-flip regions around dark times 1.5  $\mu\text{s}$ , 5.0  $\mu\text{s}$ , and 8.5  $\mu\text{s}$ .

In problems that involve the modeling of NISQ devices, another type of uncertainty arises from the inadequacy of the dynamical model of the quantum device; this is referred to as modeling uncertainty. When the dynamics is modeled by Lindblad's master equation [18], modeling uncertainty may be caused by, e.g., unknown Hamiltonian or Lindbladian operators and non-Markovian decoherence mechanisms. Violation of local conservation laws and violation of thermalization may be other sources of modeling errors [19]. Model uncertainty can limit the predictive capability<sup>1</sup> of the dynamical model; it causes a discrepancy between experimental and simulated data that can *not* be compensated for by modifying the parameters in the dynamical model.

A major difficulty that arises in modeling NISQ devices is due to the complex structure of experimental and modeling uncertainties. Moreover, it is hard to make a clear-cut distinction between the different types and sources of uncertainties, hampering their identification and treatment. Most Bayesian techniques for quantum characterization (see for example the references above) only account for experimental uncertainty and assume that it is additive and normally distributed with mean zero. This amounts to representing the experimental data by a normal random vectors where the mean equals the simulated data from the dynamical model. These techniques further assume that the chosen Hamiltonian and

<sup>1</sup>Predictive capability is the use of a computational model to predict the response of a system, in the presence of uncertainty, to conditions which the system has never experienced (and hence no experimental data are available).

Lindbladian dynamical models are capable of accurately describing the dynamics of the quantum system. Model uncertainty, however, has up to this point not been considered in the Bayesian quantum characterization literature, even though it can be a major contributor to the overall uncertainty for complex quantum systems. We proceed to demonstrate that including model uncertainty in the characterization, through a model discrepancy term that is added to the characterized dynamical model, can improve the predictive capability of quantum simulations.

Treatment of experimental and modeling uncertainty has been a challenging research topic in Bayesian statistics. Experimental uncertainty is often modeled by including additive or multiplicative random noise in the dynamical model. The idea of using a Gaussian process to represent the discrepancy between simulated and experimental data is widely credited to Kennedy and O’Hagan [20]. They propose a Bayesian framework, often referred to as the KOH framework, in which experimental data is used to simultaneously estimate the parameters in the simulation model and the hyper-parameters in the discrepancy function, given prior distributions on both. Following the seminal work of Kennedy and O’Hagan, a number of Bayesian approaches have been proposed to include model discrepancy. These approaches mainly differ in the formulation of the discrepancy, either as an “external” term that is explicitly added on top of the simulation model [21, 22, 23, 24, 25, 26, 27, 28, 29], or as an “internal” term that is embedded within the simulation model [30, 31, 32, 33]. In general, the preferred choice of approach and the treatment of the model uncertainty depends on the specific problem at hand.

In the present paper, we introduce a Bayesian quantum characterization technique that takes into account both experimental and modeling uncertainties. To fix ideas, we follow [20] and consider a Gaussian process as a prior for the model discrepancy term. We then cast the quantum characterisation problem into a Bayesian framework by deriving a multi-variate Gaussian distribution that represents the conditional distribution (or likelihood) of observing the data, given the parameters in the Lindbladian model and the hyper-parameters in the Gaussian process. In the large data-set regime the likelihood function becomes near-degenerate and computationally infeasible to evaluate. To mitigate the degeneracy, we develop two computationally efficient sampling strategies. The first approach is based on a numerically stable low-rank approximation of the likelihood function. The second technique relies on marginalizing the likelihood function over the degenerate subspace. We apply the proposed method to the characterization of a tantalum-based transmon device [17], within the QuDIT system at Lawrence Livermore National Laboratory. To illustrate how model discrepancy improves the predictive capability of Lindblad’s master equations, we compare experimental Ramsey data and simulation results, with and without model discrepancy.

The remainder of the paper is organized as follows. Section 2 describes the proposed Gaussian process-based Bayesian approach in a general setting. We then present two strategies to perform stable and fast Markov chain Monte-Carlo sampling in Sections 3 and 4. In Section 5, we apply the proposed methods to quantum characterization based on Ramsey measurements. Concluding discussions are given in Section 6.

## 2 The Gaussian process-based Bayesian approach in a general setup

We consider the uncertainty analysis and prediction of complex physical systems that are described by parametric mathematical models. The general approach consists of two steps. First, physical observations of the system are used to infer the unknown model parameters in a Bayesian framework. We refer to this step as model parameter characterization (this is called model calibration in the Bayesian statistics literature). Next, the mathematical model, with the inferred uncertain parameters, is used to make predictions about the unobserved behaviour of the physical system. We present a Bayesian

approach that accounts for experimental uncertainty as well as model uncertainty, recognizing the discrepancy between the observed data and the model predictions from the best-fitting parameter values or distributions. We employ Gaussian variables and Gaussian processes to represent the experimental noise and model discrepancy, respectively. The characterized dynamical model together with the model discrepancy are then used for predicting experimental data.

## 2.1 The inverse problem and its Bayesian formulation

Let  $\{y_1, \dots, y_n\}$  be a set of noisy experimental measurements corresponding to a set of time points  $\{t_1, \dots, t_n\}$ , with  $0 \leq t_1 < t_2 < \dots < t_n \leq T$ . Let further  $f(t_i; \theta)$  be the simulated measurement, corresponding to  $y_i$  and obtained by computing the mathematical model, with parameters  $\theta \in \Theta \subset \mathbb{R}^d$  at time  $t_i$ , that describes the physical system. For example, in the case of quantum systems,  $y_i$  may be the measured population of a certain quantum state taken at dark time  $t_i \in [0, T]$  in a Ramsey experiment, and  $f(t_i; \theta)$  may be the simulated population obtained by solving Lindblad's master equations with parameters  $\theta$ . We are hence dealing with an “inverse” problem of recovering  $\theta$  from a set of noisy observations  $\{y_i\}_{i=1}^n$  of  $\{f(t_i; \theta)\}_{i=1}^n$ .

In a Bayesian framework, we assume that  $\theta$  is random and hence characterized by a joint probability distribution that is available to us only through a set of randomly corrupted observations  $\mathbf{y}_n := \{y_i\}_{i=1}^n$ ; see e.g., [34]. Positing a likelihood function, that represents the conditional distribution of the observed data given  $\theta$ , the conditional posterior distribution of  $\theta$  is then given by Bayes' rule [35],

$$\Pr(\theta | \mathbf{y}_n) = \frac{\Pr(\mathbf{y}_n | \theta) \Pr(\theta)}{\int_{\Theta} \Pr(\mathbf{y}_n | \theta) \Pr(\theta) d\theta}.$$

Here,  $\Pr(\theta)$  is a prior distribution that expresses our belief about  $\theta$  before observing the data.

Motivated by [20], we consider the following relationship between the experimental and simulated measurements:

$$y_i = f(t_i; \theta) + \delta(t_i) + \varepsilon_i, \quad i = 1, \dots, n, \quad (1)$$

where  $\varepsilon_i$  represents the random noise in the  $i$ -th observation  $y_i$ , and  $\delta(\cdot)$  is a model discrepancy function. Following the common practice in Bayesian analysis, we assume that  $\varepsilon_i$ 's are independently and identically distributed Gaussian variables with mean zero and variance  $\sigma_\varepsilon^2$ ,

$$\varepsilon_i \sim \mathcal{N}(0, \sigma_\varepsilon^2), \quad i = 1, \dots, n.$$

We further let the discrepancy function  $\delta(\cdot)$  be modeled by a Gaussian process with a zero mean and a covariance kernel  $\kappa(t, t')$ , e.g.,

$$\delta(t) \sim \mathcal{GP}(0, \kappa(t, t')), \quad \kappa(t, t') = \sigma_\delta^2 \exp\left(-\frac{|t - t'|^\gamma}{2\ell^\gamma}\right), \quad (2)$$

with the variance  $\sigma_\delta^2$  and the time scale  $\ell$ , and with a fixed exponent  $\gamma \in [1, 2]$ . Let also  $K$  denote the  $n \times n$  matrix of the covariance kernel  $\kappa$  evaluated at all pairs of (training) time points,

$$K = [K_{i,j}] = [\kappa(t_i, t_j)] \in \mathbb{R}^{n \times n}, \quad i, j \in \{1, \dots, n\}.$$

A Gaussian process is an infinite collection of random variables, any finite number of which have a joint Gaussian distribution with a mean and covariance determined by the mean and covariance kernel (or function) of the process; see e.g., [36]. Different forms of covariance kernels can be used within a Gaussian process. The covariance kernel that we consider in (2) is often used in situations where

the correlation between data-points decreases as their separation in time increases. In the numerical experiments presented in Section 5, we consider both squared exponential (with  $\gamma = 2$ ) and exponential (with  $\gamma = 1$ ) covariance kernels. However, we note that our approach applies to general covariance kernels and is not restricted to the specific form of (2).

From the assumption that the difference between experimental and simulated data equals the sum of model discrepancy and experimental noise (see (1)), and the definition of a Gaussian process, it follows that we can view the data points  $\{y_1, \dots, y_n\}$  as the coordinates of a Gaussian random vector,

$$\mathbf{y}_n = (y_1, \dots, y_n) \sim \mathcal{N}(\mathbf{f}(\boldsymbol{\theta}), \Sigma(\boldsymbol{\alpha})),$$

with the mean vector  $\mathbf{f}(\boldsymbol{\theta}) \in \mathbb{R}^n$  and the covariance matrix  $\Sigma(\boldsymbol{\alpha}) \in \mathbb{R}^{n \times n}$  given by

$$\mathbf{f}(\boldsymbol{\theta}) = (f(t_1; \boldsymbol{\theta}), \dots, f(t_n; \boldsymbol{\theta})), \quad \Sigma(\boldsymbol{\alpha}) = K(\sigma_\delta, \ell) + \sigma_\epsilon^2 I_n.$$

Here, we have collected the reciprocal of the Gaussian noise variance  $1/\sigma_\epsilon^2$ , the reciprocal of the Gaussian process variance  $1/\sigma_\delta^2$ , and the time scale  $\ell$  of the Gaussian process in the hyper-parameter vector  $\boldsymbol{\alpha}$ ,

$$\boldsymbol{\alpha} = (1/\sigma_\epsilon^2, 1/\sigma_\delta^2, \ell).$$

The likelihood then reads

$$\Pr(\mathbf{y}_n | \boldsymbol{\theta}, \boldsymbol{\alpha}) = (2\pi)^{-n/2} |\Sigma(\boldsymbol{\alpha})|^{-1/2} \exp \left( -\frac{1}{2} (\mathbf{y}_n - \mathbf{f}(\boldsymbol{\theta}))^\top \Sigma^{-1}(\boldsymbol{\alpha}) (\mathbf{y}_n - \mathbf{f}(\boldsymbol{\theta})) \right). \quad (3)$$

Following Bayes' rule, we can write

$$\Pr(\boldsymbol{\theta}, \boldsymbol{\alpha} | \mathbf{y}_n) \propto \Pr(\mathbf{y}_n | \boldsymbol{\theta}, \boldsymbol{\alpha}) \Pr(\boldsymbol{\theta}, \boldsymbol{\alpha}). \quad (4)$$

## 2.2 A Markov Chain Monte Carlo sampling algorithm

We generate samples from parameter posteriors  $\Pr(\boldsymbol{\theta}, \boldsymbol{\alpha} | \mathbf{y}_n)$  in (4) using a Metropolis-within-Gibbs sampling strategy. The algorithm iteratively generates a sequence of samples, forming a Markov chain, whose distribution approaches the target distribution of parameters in the limit; see, e.g., [34] and the references therein for details on MCMC sampling techniques. The algorithm consists of two interactive parts: a Gibbs sampler and a Metropolis sampler. In each iteration, Gibbs sampling is employed to sample from the joint distribution  $\Pr(\boldsymbol{\theta}, \boldsymbol{\alpha} | \mathbf{y}_n)$  of the parameters by first sampling  $\boldsymbol{\alpha}$  from  $\Pr(\boldsymbol{\alpha} | \boldsymbol{\theta}, \mathbf{y}_n)$  and then sampling  $\boldsymbol{\theta}$  from  $\Pr(\boldsymbol{\theta} | \boldsymbol{\alpha}, \mathbf{y}_n)$  by utilizing two separate Metropolis steps, one for  $\boldsymbol{\alpha}$  and one for  $\boldsymbol{\theta}$ . The details of the algorithm are summarized in Algorithm 1.

**Prior distributions.** In general, the choice of prior is problem dependent and is often based on expert opinion. Assuming that model parameters and hyper-parameters are independent, we can write

$$\Pr(\boldsymbol{\theta}, \boldsymbol{\alpha}) = \Pr(\boldsymbol{\theta}) \Pr(\boldsymbol{\alpha}).$$

We then may consider different types of priors for  $\boldsymbol{\theta}$  and  $\boldsymbol{\alpha}$ , such as uniform priors, taking into account any information that may be available to us before the data is collected. For instance, we know that the hyper-parameters  $\boldsymbol{\alpha}$  are all positive, or we may have information about the range of model parameters  $\boldsymbol{\theta}$ ; see Section 5.4 for examples.

**Proposal distributions.** In the present work, we use uniform random walk proposals to generate new samples  $\tilde{\boldsymbol{\alpha}}$  and  $\tilde{\boldsymbol{\theta}}$  from current samples  $\boldsymbol{\alpha}^{(m)}$  and  $\boldsymbol{\theta}^{(m)}$ :

$$\tilde{\boldsymbol{\alpha}} \sim \text{Uniform}(\boldsymbol{\alpha}^{(m)} - \mathbf{r}_\alpha/2, \boldsymbol{\alpha}^{(m)} + \mathbf{r}_\alpha/2), \quad \tilde{\boldsymbol{\theta}} \sim \text{Uniform}(\boldsymbol{\theta}^{(m)} - \mathbf{r}_\theta/2, \boldsymbol{\theta}^{(m)} + \mathbf{r}_\theta/2), \quad (5)$$

---

**Algorithm 1** Metropolis-within-Gibbs Sampling

---

**1. Initialization:**

Select two symmetric proposals  $q_\alpha$  and  $q_\theta$ .

Select the length  $M$  of the Markov chain.

Select an arbitrary initial point  $(\theta^{(0)}, \alpha^{(0)})$  within prior's support.

**2. Gibbs sampling loop:**

**for**  $m = 0, 1, \dots, M - 1$

- Metropolis sampling step 1: draw a sample  $\alpha^{(m+1)} \sim \Pr(\alpha|\theta^{(m)}, \mathbf{y}_n)$  as follows:

- Generate a candidate sample  $\tilde{\alpha}$  drawn from a symmetric proposal distribution  $q_\alpha(\alpha^{(m)}, \tilde{\alpha})$ .
- Compute the acceptance probability

$$\gamma_\alpha = \min \left\{ 1, \frac{\Pr(\tilde{\alpha}|\theta^{(m)}, \mathbf{y}_n)}{\Pr(\alpha^{(m)}|\theta^{(m)}, \mathbf{y}_n)} \right\} = \min \left\{ 1, \frac{\Pr(\mathbf{y}_n|\theta^{(m)}, \tilde{\alpha})}{\Pr(\mathbf{y}_n|\theta^{(m)}, \alpha^{(m)})} \cdot \frac{\Pr(\theta^{(m)}, \tilde{\alpha})}{\Pr(\theta^{(m)}, \alpha^{(m)})} \right\}.$$

- Set  $\alpha^{(m+1)} = \begin{cases} \tilde{\alpha} & \text{if } \gamma_\alpha \geq u \sim \text{Uniform}(0, 1), \\ \alpha^{(m)} & \text{otherwise.} \end{cases}$

- Metropolis sampling step 2: draw a sample  $\theta^{(m+1)} \sim \Pr(\theta|\alpha^{(m+1)}, \mathbf{y}_n)$  as follows:

- Generate a candidate sample  $\tilde{\theta}$  drawn from a symmetric proposal distribution  $q_\theta(\theta^{(m)}, \tilde{\theta})$ .
- Compute the acceptance probability

$$\gamma_\theta = \min \left\{ 1, \frac{\Pr(\tilde{\theta}|\alpha^{(m+1)}, \mathbf{y}_n)}{\Pr(\theta^{(m)}|\alpha^{(m+1)}, \mathbf{y}_n)} \right\} = \min \left\{ 1, \frac{\Pr(\mathbf{y}_n|\tilde{\theta}, \alpha^{(m+1)})}{\Pr(\mathbf{y}_n|\theta^{(m)}, \alpha^{(m+1)})} \cdot \frac{\Pr(\tilde{\theta}, \alpha^{(m+1)})}{\Pr(\theta^{(m)}, \alpha^{(m+1)})} \right\}.$$

- Set  $\theta^{(m+1)} = \begin{cases} \tilde{\theta} & \text{if } \gamma_\theta \geq u \sim \text{Uniform}(0, 1), \\ \theta^{(m)} & \text{otherwise.} \end{cases}$

**end for**

**3. Output:** return  $\{\alpha^{(m)}\}_{m=1}^M$  and  $\{\theta^{(m)}\}_{m=1}^M$ .

---

where  $\mathbf{r}_\alpha$  and  $\mathbf{r}_\theta$  are two support vectors, to be selected so that the proposal distributions are neither too wide, nor too narrow. A too wide proposal would result in an acceptance rate close to zero, and the chain would rarely move to a different sample, while a too narrow proposal would result in an acceptance rate close to one, but the generated samples would not cover the support of the actual posterior distribution. If a proposal gives a new sample outside the support of the prior, we may simply discard the sample and draw another sample from the proposal. It is to be noted that the choice (5) induces symmetric proposals, i.e.,  $q_\alpha(\alpha^{(m)}, \tilde{\alpha}) = q_\alpha(\tilde{\alpha}, \alpha^{(m)})$  and  $q_\theta(\theta^{(m)}, \tilde{\theta}) = q_\theta(\tilde{\theta}, \theta^{(m)})$ . If, instead of symmetric proposals, we opted for non-symmetric proposals, then we would need to multiply the acceptance ratios

in  $\gamma_\alpha$  and  $\gamma_\theta$  by  $q_\alpha(\alpha^{(m)}, \tilde{\alpha})/q_\alpha(\tilde{\alpha}, \alpha^{(m)})$  and  $q_\theta(\theta^{(m)}, \tilde{\theta})/q_\theta(\tilde{\theta}, \theta^{(m)})$ , respectively. This would in turn require extra evaluations of proposals.

**Deterministic hyper-parameters.** After generating independent samples from the posterior distribution  $\Pr(\theta, \alpha | \mathbf{y})$ , we compute the mean (or alternatively the mode) of the posterior samples of the hyper-parameters  $\alpha$ . This gives us a deterministic variance, say  $\hat{\sigma}_\varepsilon^2$ , for the noise  $\varepsilon$  and a deterministic covariance kernel, say  $\hat{\kappa}(t_i, t_j)$ , for the model discrepancy  $\delta$ . The posterior samples of the model parameters  $\theta$  will be retained for making predictions, as we describe next.

## 2.3 Gaussian process predictions

After the noisy measurements  $\mathbf{y}_n = (y_1, \dots, y_n)$  at a set of *training* points  $\mathbf{t} = (t_1, \dots, t_n)$  are collected and independent samples from parameter posteriors  $\Pr(\theta | \mathbf{y}_n)$  are obtained, we may wish to make predictions by the inferred parameterized model  $f(\cdot; \theta)$  and its discrepancy  $\delta(\cdot)$  at a new set of *test* points  $\mathbf{t}^* = (t_1^*, \dots, t_{n^*}^*)$ . To this end, we first write

$$\mathbf{g}^* = (g(t_1^*), \dots, g(t_{n^*}^*)), \quad g(t_i^*) := f(t_i^*; \theta) + \delta(t_i^*), \quad i = 1, \dots, n^*.$$

Note that  $\mathbf{g}^*$  is a random vector that depends on the random vector  $\mathbf{y}_n$  of noisy measurements. Also, note that in general the number of test points may be different from the number of training points,  $n^* \neq n$ . The goal of prediction is hence to obtain the distribution of  $\mathbf{g}^*$  conditional on  $\mathbf{y}_n$ .

**Case I.** We first consider the simple case when  $\theta$  is deterministic; for instance we may take the mean or mode of the posterior samples of  $\theta$  obtained by Algorithm 1. This may be a valid practice for example when the parameters' posterior is very concentrated so that their uncertainty can be ignored. In this case, both  $\mathbf{y}_n$  and  $\mathbf{g}^*$  are Gaussian random vectors with the Gaussian joint distribution

$$\begin{bmatrix} \mathbf{y}_n \\ \mathbf{g}^* \end{bmatrix} \sim \mathcal{N} \left( \begin{bmatrix} \mathbf{f}(\theta) \\ \mathbf{f}^*(\theta) \end{bmatrix}, \begin{bmatrix} \hat{K} + \hat{\sigma}_\varepsilon^2 I_n & \hat{K}^* \\ \hat{K}^{*\top} & \hat{K}^{**} \end{bmatrix} \right),$$

where

$$\mathbf{f}(\theta) := (f(t_1; \theta), \dots, f(t_n; \theta)) \in \mathbb{R}^n, \quad \mathbf{f}^*(\theta) := (f(t_1^*; \theta), \dots, f(t_{n^*}^*; \theta)) \in \mathbb{R}^{n^*},$$

and

$$\hat{K} = [\hat{\kappa}(t_i, t_j)] \in \mathbb{R}^{n \times n}, \quad \hat{K}^* = [\hat{\kappa}(t_i, t_j^*)] \in \mathbb{R}^{n \times n^*}, \quad \hat{K}^{**} = [\hat{\kappa}(t_i^*, t_j^*)] \in \mathbb{R}^{n^* \times n^*}.$$

The conditional distribution is then given by

$$\mathbf{g}^* | \mathbf{y}_n \sim \mathcal{N} \left( \mathbf{f}^*(\theta) + A(\mathbf{y}_n - \mathbf{f}(\theta)), \hat{K}^{**} - A \hat{K}^* \right), \quad A := \hat{K}^{*\top} (\hat{K} + \sigma_\varepsilon^2 I_n)^{-1}.$$

**Case II.** Next, we consider the case when  $\theta$  is random, and as a result, the contribution of its uncertainty to  $\mathbf{f}(\theta)$  and  $\mathbf{f}^*(\theta)$  and hence to the predictive conditional distribution of  $\mathbf{g}^*$  needs to be accounted for. Provided the posterior distribution of  $\theta$  is unimodal and assuming that  $f(\cdot; \theta)$  at any training or test time point follows a Gaussian distribution, we get the joint distribution

$$\begin{bmatrix} \mathbf{y}_n \\ \mathbf{g}^* \end{bmatrix} \sim \mathcal{N} \left( \begin{bmatrix} \bar{\mathbf{f}}_\theta \\ \bar{\mathbf{f}}_\theta^* \end{bmatrix}, \begin{bmatrix} K_\theta + \hat{K} + \hat{\sigma}_\varepsilon^2 I_n & K_\theta^* + \hat{K}^* \\ K_\theta^{*\top} + \hat{K}^{*\top} & K_\theta^{**} + \hat{K}^{**} \end{bmatrix} \right),$$

where

$$\bar{\mathbf{f}}_{\boldsymbol{\theta}} := \mathbb{E}[(f(t_1; \boldsymbol{\theta}), \dots, f(t_n; \boldsymbol{\theta}))] \in \mathbb{R}^n, \quad \bar{\mathbf{f}}_{\boldsymbol{\theta}}^* := \mathbb{E}[(f(t_1^*; \boldsymbol{\theta}), \dots, f(t_{n^*}^*; \boldsymbol{\theta}))] \in \mathbb{R}^{n^*},$$

and

$$K_{\boldsymbol{\theta}} = [\text{cov}(f(t_i; \boldsymbol{\theta}), f(t_j; \boldsymbol{\theta}))], \quad K_{\boldsymbol{\theta}}^* = [\text{cov}(f(t_i; \boldsymbol{\theta}), f(t_j^*; \boldsymbol{\theta}))], \quad K_{\boldsymbol{\theta}}^{**} = [\text{cov}(f(t_i^*; \boldsymbol{\theta}), f(t_j^*; \boldsymbol{\theta}))].$$

These expectations and covariances can be approximated by MC sampling using the independent samples of parameter posteriors obtained by the MCMC algorithm. The conditional distribution is then given by

$$\mathbf{g}^* | \mathbf{y}_n \sim \mathcal{N}(\bar{\mathbf{f}}_{\boldsymbol{\theta}}^* + B(\mathbf{y}_n - \bar{\mathbf{f}}_{\boldsymbol{\theta}}), K_{\boldsymbol{\theta}}^{**} + \hat{K}^{**} - B(K_{\boldsymbol{\theta}}^* + \hat{K}^*)), \quad B := (K_{\boldsymbol{\theta}}^{*\top} + \hat{K}^{*\top})(K_{\boldsymbol{\theta}} + \hat{K} + \sigma_{\varepsilon}^2 I_n)^{-1}.$$

### 3 A low-rank approximate likelihood approach for large data sets

In the case of large data sets ( $n \gg 1$ ), two issues may arise in computing the likelihood (3) that appears in each iteration of Algorithm 1. First, it becomes computationally intractable; the cost of computing the inverse and determinant of  $\Sigma(\boldsymbol{\alpha}) \in \mathbb{R}^{n \times n}$  at each iteration of the algorithm grows cubically with  $n$ . Secondly, and more critically, as the time points gets closer to each other, the covariance matrix  $\Sigma(\boldsymbol{\alpha})$  becomes more degenerate and its determinant becomes exponentially small, leading to numerical round off errors. To mitigate these problems, we propose a stable low-rank approximation of the Gaussian likelihood (3) when the covariance matrix  $\Sigma(\boldsymbol{\alpha})$  is given by the sum of a squared exponential kernel matrix (with  $\gamma = 2$ ) and a diagonal matrix,

$$\Sigma(\boldsymbol{\alpha}) = K(\sigma_{\delta}, \ell) + \sigma_{\varepsilon}^2 I_n, \quad K(\sigma_{\delta}, \ell) = [\sigma_{\delta}^2 \exp(-(t_i - t_j)^2 / (2\ell^2))].$$

The first step is to build a low-rank approximation of the squared exponential covariance matrix  $K \in \mathbb{R}^{n \times n}$  by truncating the eigen-expansion of the squared exponential covariance kernel  $k(t, t') = \exp(-(t - t')^2 / (2\ell^2))$ . To this end, we recall that by Mercer's theorem (see e.g., Theorem 4.2 in [36]), given a finite measure  $\mu$  on  $\mathbb{R}$ , we have  $\mu^2$ -almost everywhere,

$$k(t, t') = \sum_{j=1}^{\infty} \lambda_j \phi_j(t) \phi_j(t'), \quad \int_{\mathbb{R}} k(t, t') \phi(t) d\mu(t) = \lambda \phi(t').$$

In the case when  $\mu$  is a Gaussian measure, i.e.,  $d\mu(t) = p(t)dt$  with  $p(t) = \mathcal{N}(t | 0, \sigma^2)$ , we have analytical formulas for the eigenpairs  $(\lambda, \phi)$  of the squared exponential covariance kernel (see [37]):

$$\lambda_j = \sqrt{\frac{2}{1 + \beta + \sqrt{1 + 2\beta}}} \left( \frac{\beta}{1 + \beta + \sqrt{1 + 2\beta}} \right)^{j-1}, \quad j = 1, 2, \dots,$$

$$\phi_j(t) = \frac{(1 + 2\beta)^{1/8}}{\sqrt{2^{j-1}(j-1)!}} \exp\left(-\frac{\sqrt{1 + 2\beta} - 1}{4\sigma^2} t^2\right) H_{j-1}\left(\frac{1}{\sigma} \left(\frac{1}{4} + \frac{\beta}{2}\right)^{1/4} t\right), \quad j = 1, 2, \dots,$$

where  $\beta := 2\sigma^2/\ell^2$ , and  $H_i$  is the  $i$ -th order Hermite polynomial. Due to the fast decay of the eigenvalues, we can generate a low-rank approximation  $\tilde{K}$  of the covariance matrix  $K$  by retaining only  $r \ll n$  terms of the covariance kernel expansion,

$$K \approx \tilde{K} = U U^{\top}, \quad U = [\mathbf{u}_1, \dots, \mathbf{u}_r] \in \mathbb{R}^{n \times r}, \quad \mathbf{u}_j = \sigma_{\delta} \sqrt{\lambda_j} [\phi_j(t_1), \dots, \phi_j(t_n)]^{\top} \in \mathbb{R}^n.$$



The next step is to replace the covariance matrix  $\Sigma = K + \sigma_\varepsilon^2 I_n$  by its approximation  $\tilde{\Sigma} = \tilde{K} + \sigma_\varepsilon^2 I_n$  and compute the inverse and determinant of  $\tilde{\Sigma}$  as follows. The inverse is obtained by the Woodbury matrix identity [38],

$$\tilde{\Sigma}^{-1} = (UU^\top + \sigma_\varepsilon^2 I_n)^{-1} = \sigma_\varepsilon^{-2} I_n - \sigma_\varepsilon^{-4} U(I_r + \sigma_\varepsilon^{-2} U^\top U)^{-1} U^\top.$$

We note that the formula in the right hand side of the above identity requires the inversion of a small  $r \times r$  matrix. The overall complexity of computing the inverse of  $\tilde{\Sigma}$  is hence  $\mathcal{O}(rn + r^3)$ , which is much less than the cost  $\mathcal{O}(n^3)$  of inverting the original matrix  $\Sigma$  when  $r \ll n$ .

In order to compute the determinant of  $\tilde{\Sigma}$ , we first note that since  $\tilde{K}$  is a symmetric positive semidefinite matrix with rank  $r \ll n$ , it has  $r$  positive eigenvalues  $\tilde{\lambda}_1 \geq \tilde{\lambda}_2 \geq \dots \geq \tilde{\lambda}_r > 0$  and  $n - r$  zero eigenvalues. Further, it has a complete set of orthonormal eigenvectors,

$$\tilde{K} = Q \Lambda Q^\top, \quad Q Q^\top = I_n, \quad \Lambda = \text{diag}(\tilde{\lambda}_1, \dots, \tilde{\lambda}_r, 0, \dots, 0).$$

This implies

$$\tilde{\Sigma} = \tilde{K} + \sigma_\varepsilon^2 I_n = Q \Gamma Q^\top, \quad \Gamma := \Lambda + \sigma_\varepsilon^2 I_n = \text{diag}(\tilde{\lambda}_1 + \sigma_\varepsilon^2, \dots, \tilde{\lambda}_r + \sigma_\varepsilon^2, \sigma_\varepsilon^2, \dots, \sigma_\varepsilon^2),$$

and hence

$$|\tilde{\Sigma}| = |\Gamma| = \sigma_\varepsilon^{2(n-r)} \prod_{j=1}^r (\tilde{\lambda}_j + \sigma_\varepsilon^2).$$

The above formulae only requires computing the  $r$  largest (positive) eigenvalues of the matrix  $\tilde{K}$ , which can efficiently be done by a randomized QR factorization algorithm; see [39]. The upshot of the low-rank approximation of  $K$  is the approximate likelihood formula:

$$\tilde{P}_R(\mathbf{y}_n | \boldsymbol{\theta}, \boldsymbol{\alpha}) = (2\pi)^{-n/2} |\tilde{\Sigma}(\boldsymbol{\alpha})|^{-1/2} \exp \left( -\frac{1}{2} (\mathbf{y}_n - \mathbf{f}(\boldsymbol{\theta}))^\top \tilde{\Sigma}^{-1}(\boldsymbol{\alpha}) (\mathbf{y}_n - \mathbf{f}(\boldsymbol{\theta})) \right),$$

where  $|\tilde{\Sigma}(\boldsymbol{\alpha})|$  and  $\tilde{\Sigma}^{-1}(\boldsymbol{\alpha})$  are obtained as described above.

We finally note that more general covariance kernels could be handled without knowledge of their eigenfunction expansion, for example using the Nyström method [40].

## 4 A marginalized likelihood approach for large data sets

In this section, we propose an alternative approach to the low-rank likelihood approach presented in Section 3. The alternative approach utilizes the eigen-decomposition of the covariance matrix  $\Sigma(\boldsymbol{\alpha})$  to decompose its range (or column space) into two sub-spaces, one spanned by the eigenvectors corresponding to large eigenvalues and one spanned by the eigenvectors corresponding to small eigenvalues. We then orthogonally project all random variables onto these two sub-spaces and marginalize out the random variables belonging to the sub-space corresponding to the small eigenvalues. The advantage of this approach over the one presented in Section 3 is that it does not rely on the eigen-expansion of the covariance kernel and is hence applicable to more general covariance kernels. On the other hand, it requires computing the eigenvectors of the covariance matrix corresponding to the large eigenvalues that are retained.

We first note that Algorithm 1 requires many evaluations of the likelihood function (3) at the data set  $\mathbf{y}_n$ , for many different values of the parameter vector  $(\boldsymbol{\theta}, \boldsymbol{\alpha})$ . For the ease of exposition, we drop the

parameters  $\boldsymbol{\theta}$  and  $\boldsymbol{\alpha}$  and set  $\mathbf{x} := \mathbf{y}_n - \mathbf{f}(\boldsymbol{\theta})$  and  $\Sigma := \Sigma(\boldsymbol{\alpha})$ . We then consider the likelihood function (3) in the following condensed form

$$L(\mathbf{x}) = \frac{1}{C} \exp\left(-\frac{1}{2}\mathbf{x}^\top \Sigma^{-1} \mathbf{x}\right), \quad C = \int_{\mathbb{R}^n} \exp\left(-\frac{1}{2}\mathbf{x}^\top \Sigma^{-1} \mathbf{x}\right) d\mathbf{x}.$$

As mentioned earlier, the covariance matrix  $\Sigma \in \mathbb{R}^{n \times n}$  is almost degenerate, with many small eigenvalues, and hence a direct computation of its determinant and inverse may lead to numerical instabilities and becomes impractical. Nevertheless, since the covariance matrix is symmetric and positive definite, it has real and positive eigenvalues with a complete set of orthonormal eigenvectors. The covariance matrix therefore satisfies the eigen-decomposition

$$\Sigma = E\Lambda E^\top, \quad E^\top E = I_n, \quad \Lambda = \begin{bmatrix} \Lambda_I & 0 \\ 0 & \Lambda_{II} \end{bmatrix}, \quad E = [E_I \quad E_{II}],$$

where the diagonal matrices  $\Lambda_I = \text{diag}(\lambda_1, \dots, \lambda_r)$  and  $\Lambda_{II} = \text{diag}(\lambda_{r+1}, \dots, \lambda_n)$  hold the eigenvalues arranged in descending order, such that all eigenvalues in  $\Lambda_{II}$  are small,  $1 \gg \lambda_{r+1} \geq \dots \geq \lambda_n > 0$ , and  $E_I \in \mathbb{R}^{n \times r}$  and  $E_{II} \in \mathbb{R}^{n \times (n-r)}$  hold the corresponding eigenvectors.

Next, we note that in order to evaluate  $L(\mathbf{x})$  we need to solve the linear system  $\Sigma \mathbf{z} = \mathbf{x}$ . For this purpose we introduce the orthogonal projection matrices

$$P_I = E_I E_I^\top, \quad P_{II} = E_{II} E_{II}^\top, \quad P_I + P_{II} = I_n,$$

and decompose the vectors  $\mathbf{x} = P_I \mathbf{x} + P_{II} \mathbf{x}$  and  $\mathbf{z} = P_I \mathbf{z} + P_{II} \mathbf{z}$ :

$$\begin{aligned} \mathbf{x} &= E_I \mathbf{x}_I + E_{II} \mathbf{x}_{II}, & \mathbf{x}_I &= E_I^\top \mathbf{x} \in \mathbb{R}^r, & \mathbf{x}_{II} &= E_{II}^\top \mathbf{x} \in \mathbb{R}^{n-r}, \\ \mathbf{z} &= E_I \mathbf{z}_I + E_{II} \mathbf{z}_{II}, & \mathbf{z}_I &= E_I^\top \mathbf{z} \in \mathbb{R}^r, & \mathbf{z}_{II} &= E_{II}^\top \mathbf{z} \in \mathbb{R}^{n-r}. \end{aligned}$$

It is easy to see that the linear system  $\Sigma \mathbf{z} = \mathbf{x}$ , or equivalently  $\Lambda E^\top \mathbf{z} = E^\top \mathbf{x}$ , decomposes into two smaller linear systems with diagonal matrices,

$$\Lambda_I \mathbf{z}_I = \mathbf{x}_I, \quad \Lambda_{II} \mathbf{z}_{II} = \mathbf{x}_{II}.$$

Hence, the solution to the linear system  $\Sigma \mathbf{z} = \mathbf{x}$  can be written as

$$\mathbf{z} = E_I \mathbf{z}_I + E_{II} \mathbf{z}_{II}, \quad \mathbf{z}_I = \Lambda_I^{-1} E_I^\top \mathbf{x}, \quad \mathbf{z}_{II} = \Lambda_{II}^{-1} E_{II}^\top \mathbf{x}.$$

The likelihood function can be decomposed according to

$$\begin{aligned} L(\mathbf{x}) &= \frac{1}{C} \exp\left(-\frac{1}{2}\mathbf{x}^\top \Sigma^{-1} \mathbf{x}\right) = \frac{1}{C} \exp\left(-\frac{1}{2}\mathbf{x}^\top \mathbf{z}\right) \\ &= \frac{1}{C} \exp\left(-\frac{1}{2}\mathbf{x}^\top (E_I \Lambda_I^{-1} E_I^\top \mathbf{x} + E_{II} \Lambda_{II}^{-1} E_{II}^\top \mathbf{x})\right) \\ &= \underbrace{\frac{1}{C_I} \exp\left(-\frac{1}{2}\mathbf{x}_I^\top \Lambda_I^{-1} \mathbf{x}_I\right)}_{L_I(\mathbf{x}_I)} \underbrace{\frac{1}{C_{II}} \exp\left(-\frac{1}{2}\mathbf{x}_{II}^\top \Lambda_{II}^{-1} \mathbf{x}_{II}\right)}_{L_{II}(\mathbf{x}_{II})}, \end{aligned}$$

where  $C_I = (2\pi)^{r/2} |\Lambda_I|^{1/2}$  and  $C_{II} = (2\pi)^{(n-r)/2} |\Lambda_{II}|^{1/2}$ . In other words, we have written the Gaussian likelihood function  $L$  as the product of two Gaussian density functions  $L_I$  and  $L_{II}$ . It remains to note that while the computation of  $L_I(\mathbf{x}_I)$  with  $\mathbf{x}_I = E_I^\top \mathbf{x}$  is stable and efficient (when

$r \ll n$ ), the computation of  $L_{II}(\mathbf{x}_{II})$  with  $\mathbf{x}_{II} = E_{II}^\top \mathbf{x}$  may suffer from numerical instabilities. Specifically, since the diagonal elements of  $\Lambda_{II}$  are very small, computing its inverse and determinant will be intractable due to round-off errors. To avoid numerical instabilities, we marginalize the joint likelihood function  $L(\mathbf{x}) = L_I(\mathbf{x}_I) L_{II}(\mathbf{x}_{II})$  over  $\mathbf{x}_{II} \in \mathbb{R}^{n-r}$ , arriving at the marginal likelihood  $L_I(\mathbf{x}_I) = \int_{\mathbb{R}^{n-r}} L_I(\mathbf{x}_I) L_{II}(\mathbf{x}_{II}) d\mathbf{x}_{II}$ . Since  $\Lambda_I$  is of small size and does *not* have small eigenvalues, the marginal likelihood can be efficiently evaluated without numerical round-off problems, even when the covariance matrix  $\Sigma$  is arbitrarily close to being singular.

The above procedure amounts to replacing the original likelihood function (3) by:

$$\widehat{\text{Pr}}(\mathbf{y}_n | \boldsymbol{\theta}, \boldsymbol{\alpha}) = (2\pi)^{-r/2} |\Lambda_I(\boldsymbol{\alpha})|^{-1/2} \exp \left( -\frac{1}{2} \left( E_I^\top(\boldsymbol{\alpha})(\mathbf{y}_n - \mathbf{f}(\boldsymbol{\theta})) \right)^\top \Lambda_I^{-1}(\boldsymbol{\alpha}) \left( E_I^\top(\boldsymbol{\alpha})(\mathbf{y}_n - \mathbf{f}(\boldsymbol{\theta})) \right) \right),$$

where  $\Lambda_I(\boldsymbol{\alpha})$  and  $E_I(\boldsymbol{\alpha})$  contain the  $r$  largest eigenvalues and corresponding eigenvectors of the covariance matrix  $\Sigma(\boldsymbol{\alpha})$ .

## 5 Application to quantum characterization

In this section, we discuss the deployment of the proposed Bayesian approach to the quantum characterization of a superconducting device using Ramsey measurements.

### 5.1 Ramsey experimental setup and measurements

The experiments in this study are performed on a tantalum-based superconducting transmon device [17] at LLNL. In principle, a transmon can support many energy levels. However, on this system only the three lowest levels, corresponding to the states  $|0\rangle$ ,  $|1\rangle$  and  $|2\rangle$ , can be reliably measured. In the following, the transmon device will be referred to as the “qudit”. For simplicity, we limit our discussion to the Ramsey experimental protocol, which is designed to determine the transition frequencies  $\omega_{k,k+1}$  and the  $T_{2,k}^*$  dephasing time scales, also known as combined decoherence time scales [41], with  $k = 0, 1, \dots$ . Here, the frequency  $\omega_{k,k+1}$  corresponds to transition between the states  $|k\rangle$  and  $|k+1\rangle$ . Because only the first three states ( $|0\rangle$ ,  $|1\rangle$  and  $|2\rangle$ ) can be accurately measured on the qudit, we limit the experiments to determine the  $0 \leftrightarrow 1$  and  $1 \leftrightarrow 2$  transition frequencies as well as the corresponding dephasing times.

During each shot of the Ramsey  $k \leftrightarrow k+1$  experiment, we first apply a series of  $\pi$ -pulses to prepare the qudit in state  $|k\rangle$ , followed by a detuned  $\frac{\pi}{2}$ -pulse to bring the device into a superposition of states  $|k\rangle$  and  $|k+1\rangle$ . The system is then evolved freely (without applying any control pulses) during the dark time  $t_{\text{dark}}$ , after which a second detuned  $\frac{\pi}{2}$ -pulse is applied. Finally, the resulting state of the system is measured; see the appendix of [15] for details. Each Ramsey experiment is performed for  $n = 500$  dark times, discretized on a uniform grid with a step size of  $\Delta t = 20$  ns, and we perform 1,000 shots for each dark time. To setup the Ramsey experiment, the drive frequency (which determines the amount of detuning) is chosen as the estimated transition frequency from a standard calibration procedure, reduced by a 1 MHz nominal detuning. This procedure resulted in the drive frequencies  $\omega_d/2\pi = 3.4476698$  GHz and  $\omega_d/2\pi = 3.2392576$  GHz, for the  $0 \leftrightarrow 1$  and  $1 \leftrightarrow 2$  Ramsey experiments, respectively; see, e.g., [42] for details. Results from the Ramsey experiments are presented in Figure 1. In the population data for the  $1 \leftrightarrow 2$  Ramsey experiment, we note a beating and a phase flip around dark times 1.5  $\mu\text{s}$ , 5.0  $\mu\text{s}$ , and 8.5  $\mu\text{s}$ , which we attribute to parity events [43]. These random events occur on a time scale of milliseconds and alternate the transition frequencies of the device through sudden changes in the charge parity. The perturbation of the transition frequency is called the charge dispersion. Because the population data oscillates with detuning frequency  $\Delta_k = \omega_{k,k+1} - \omega_d$ , it is expected that the Fourier

spectrum of the population data will exhibit a maximum at the detuning frequency. As reported by Peng et al. [15] (also see [44]), a single peak is observed in the  $0 \leftrightarrow 1$  spectrum, but two distinctive peaks are present in the  $1 \leftrightarrow 2$  case. Given these results, we conclude that charge dispersion is significant only in the latter case.

## 5.2 Forward mathematical models

To take Markovian interaction with the environment into account we model the dynamics of the qudit using Lindblad's master equation [18, 45], which can be written on the general form:

$$\dot{\rho} = -i(H(t)\rho - \rho H(t)) + \sum_{j=1}^{N^2-1} \left( \mathcal{L}_j \rho \mathcal{L}_j^\dagger - \frac{1}{2} \left( \mathcal{L}_j^\dagger \mathcal{L}_j \rho + \rho \mathcal{L}_j^\dagger \mathcal{L}_j \right) \right). \quad (6)$$

Here,  $\rho = \rho^\dagger$  is the density matrix,  $H = H^\dagger$  is the Hamiltonian and  $\mathcal{L}_j$  denotes a decoherence operator. These operators are all in  $\mathbb{C}^{N \times N}$ , with  $N$  being the size of the Hilbert space. Only the three lowest energy levels can be reliably measured on the qudit, but to reduce artificial effects from truncation of the Hilbert space, we add a guard level and include the four lowest energy levels of the system in our modeling. Hence, we set  $N = 4$ .

The Hamiltonian operator in Lindblad's equation (6) is of the form  $H(t) = H_s + H_c(t)$ , with the system Hamiltonian  $H_s$  and the control Hamiltonian  $H_c(t)$  given by

$$H_s = \begin{pmatrix} 0 & 0 & 0 & 0 \\ 0 & \omega_{0,1} & 0 & 0 \\ 0 & 0 & \omega_{0,1} + \omega_{1,2} & 0 \\ 0 & 0 & 0 & \omega_{0,1} + \omega_{1,2} + \omega_{2,3} \end{pmatrix},$$

and

$$H_c(t) = h(t)(a + a^\dagger), \quad h(t) = 2I(t) \cos(\omega_d t) + 2Q(t) \sin(\omega_d t).$$

Here,  $a$  and  $a^\dagger$  are the lowering and raising operators,  $\omega_d$  is the angular drive frequency, and  $h(t)$  is the control function given in terms of two slowly varying envelope functions  $I$  and  $Q$ , referred to as the in-phase and the quadrature components, respectively.

These components are typically used as input signals to an IQ-mixer that, in turn, generates the control signal  $h(t)$  that is sent to the qudit.

We consider two decoherence operators<sup>2</sup> in Lindblad's equation (6): the decay operator  $\mathcal{L}_1$  and the dephasing operator  $\mathcal{L}_2$ , defined as

$$\mathcal{L}_1 = \begin{pmatrix} 0 & \sqrt{\gamma_{1,1}} & 0 & 0 \\ 0 & 0 & \sqrt{\gamma_{1,2}} & 0 \\ 0 & 0 & 0 & \sqrt{\gamma_{1,3}} \\ 0 & 0 & 0 & 0 \end{pmatrix}, \quad \mathcal{L}_2 = \begin{pmatrix} 0 & 0 & 0 & 0 \\ 0 & \sqrt{\gamma_{2,1}} & 0 & 0 \\ 0 & 0 & \sqrt{\gamma_{2,2}} & 0 \\ 0 & 0 & 0 & \sqrt{\gamma_{2,3}} \end{pmatrix}.$$

The parameter  $\gamma_{1,k}$  is the decay rate for state  $|k\rangle$ , with corresponding decay time  $T_{1,k} = 1/\gamma_{1,k}$ . The dephasing rates  $\gamma_{2,k}$  are related to the pure dephasing times  $T_{2,k}$  through the relations,  $\gamma_{2,0} = 0$ ,  $\sqrt{\gamma_{2,k}} = \sqrt{\gamma_{2,k-1}} + \sqrt{2/T_{2,k}}$ ,  $k = 1, 2, 3$ ; see the appendix of [46] for details. The pure and combined decoherence times are related by  $1/T_{2,k}^* = 1/(2T_{1,k}) + 1/T_{2,k}$ ; see [41, 46].

<sup>2</sup>Although with  $N = 4$ , there could theoretically be up to  $N^2 - 1 = 15$  Lindbladian operators, the two operators considered here are the most important ones.

The equations above are stated in the laboratory frame of reference. However, as the transition and drive frequencies are high, typically in the GHz range, numerical simulations can be computationally expensive. We slow down the time scales in the density matrix by applying the rotating wave approximation (RWA) and transforming (6) into a frame rotating with the angular frequency  $\omega_d$ ; see for example [47]. In the present work, we only use control functions that are piece-wise constant in the rotating frame of reference. Because the Hilbert space is low-dimensional, a highly efficient approach for integrating Lindblad's master equation is through matrix exponentiation.

The parity event in the  $1 \leftrightarrow 2$  transition frequency is modeled by

$$\omega_{1,2} = \bar{\omega}_{1,2} + p \epsilon_{1,2}, \quad p \in \{-1, 1\},$$

where  $\bar{\omega}_{1,2}$  is the average  $1 \leftrightarrow 2$  transition frequency,  $\epsilon_{1,2}$  is the charge dispersion and  $p \in \{-1, 1\}$  is a discrete random variable, called the parity, taking values  $\pm 1$  with equal probability [43]. We define the frequencies corresponding to the positive and negative parities as

$$\omega_{1,2}^{\pm} = \bar{\omega}_{1,2} \pm \epsilon_{1,2}.$$

Since  $p$  is assumed to be a discrete random variable with zero mean, the average  $1 \leftrightarrow 2$  transition frequency and the charge dispersion are  $\bar{\omega}_{1,2} = \frac{1}{2}(\omega_{1,2}^+ + \omega_{1,2}^-)$  and  $\epsilon_{1,2} = \frac{1}{2}(\omega_{1,2}^+ - \omega_{1,2}^-)$ , respectively.

Parity events have been reported to occur on a time scale of milliseconds [43]. This time scale is much longer than the duration of a single shot of the experiments, which typically only requires a few microseconds. Although a parity event could occur during a single shot, the disparate time scales indicate that this would be unlikely. On the other hand, the state population is often measured by averaging over 1,000 (or more) shots. In our experiments the wait time between successive shots for the same dark time varies between 0.05 ms and 0.1 ms. As a result it is likely that about half of the shots are performed for each parity. To account for both parities we solve Lindblad's master equation twice, once with  $\omega_{1,2}^+$  and once with  $\omega_{1,2}^-$ , resulting in the density matrices  $\rho^+$  and  $\rho^-$ , respectively. The average of these density matrices is then used in the characterization, described below.

### 5.3 Gaussian process-based Bayesian characterization

Let the unknown parameters of Lindblad's master equation (6) consist of the transition frequencies and the pure dephasing time scales,

$$\theta = (\omega_{0,1}, \omega_{1,2}^-, \omega_{1,2}^+, T_{2,1}, T_{2,2}).$$

Since the  $T_1$ -decay times cannot be characterized by Ramsey experiments, we assume they are already determined by some other protocol, e.g., energy decay experiments. Here, we use the fixed values  $T_{1,1} = 258.39 \mu\text{s}$  and  $T_{1,2} = 100.79 \mu\text{s}$  from [15].

In the following, let  $p_s^{(k)}(t_i)$  be the measured population of state  $s \in \{0, 1, 2\}$ , recorded at dark time  $t_i$  in the Ramsey  $k \leftrightarrow k+1$  experiment, with  $k = 0, 1$ . We collect measurements corresponding to  $n = 500$  dark times  $t_i = i \Delta t$ , with  $\Delta t = 20 \text{ ns}$  and  $i = 1, 2, \dots, n$ . Also, let  $\hat{p}_s^{(k)}(t_i; \theta)$  be the corresponding simulated populations obtained by Lindblad's master equation with parameters  $\theta$ .

Following the Bayesian approach in Section 2 and analogous to the noise-discrepancy model (1), we consider the following relationships between the experimental and simulated measurements for the two Ramsey experiments:

$$p_s^{(0)}(t_i) = \hat{p}_s^{(0)}(t_i; \theta) + \delta^{(0)}(t_i) + \varepsilon^{(0)}, \quad s = 0, 1, 2, \quad i = 1, 2, \dots, n, \quad (7)$$

$$p_s^{(1)}(t_i) = \hat{p}_s^{(1)}(t_i; \theta) + \delta^{(1)}(t_i) + \varepsilon^{(1)}, \quad s = 0, 1, 2, \quad i = 1, 2, \dots, n, \quad (8)$$

where

$$\varepsilon^{(k)} \sim \mathcal{N}(0, \sigma_{\varepsilon, k}^2), \quad \delta^{(k)}(t) \sim \mathcal{GP}(0, \kappa^{(k)}(t, t')), \quad \kappa^{(k)}(t, t') = \sigma_{\delta, k}^2 \exp\left(-\frac{|t - t'|^\gamma}{2 \ell_k^\gamma}\right), \quad k = 0, 1. \quad (9)$$

We note that since the Ramsey  $k \leftrightarrow k + 1$  measurements have different noise-discrepancy structures for different  $k \in \{0, 1\}$ , as can be seen in Figure 1, we consider different noise-discrepancy parameters  $\alpha^{(0)} = (1/\sigma_{\varepsilon, 0}^2, 1/\sigma_{\delta, 0}^2, \ell_0)$  and  $\alpha^{(1)} = (1/\sigma_{\varepsilon, 1}^2, 1/\sigma_{\delta, 1}^2, \ell_1)$  across the two Ramsey experiments. Within each Ramsey experiment, however, we assume that the noise and model discrepancy have the same covariance structures. The power in the exponent,  $\gamma \in [1, 2]$ , determines the smoothness of the Gaussian process and may also be considered as a hyper-parameter. In the following, we will however only perform numerical experiments with the fixed values  $\gamma = 2$  and  $\gamma = 1$ ; see Sections 5.4.2 and 5.4.3, respectively.

We further note that the three components  $p_0^{(k)}(t), p_1^{(k)}(t), p_2^{(k)}(t)$  represent the probabilities that a measurement taken at dark time  $t$  results in one of the three outcomes  $\{0, 1, 2\}$ . As a result, they (approximately) sum up to one at every dark time. This implies that in each Ramsey  $k \leftrightarrow k + 1$  experiment, one of the three components may not be informative and hence may be excluded from the data set. For this reason, we exclude  $p_2^{(0)}$  in the Ramsey  $0 \leftrightarrow 1$  model (7) and  $p_0^{(1)}$  in the Ramsey  $1 \leftrightarrow 2$  model (8), noting that they are much smaller than the other probability components; see Figure 1.

Now, setting

$$\begin{aligned} \mathbf{p}_s^{(0)} &= \{p_s^{(0)}(t_i)\}_{i=1}^n, & \hat{\mathbf{p}}_s^{(0)}(\boldsymbol{\theta}) &= \{\hat{p}_s^{(0)}(t_i; \boldsymbol{\theta})\}_{i=1}^n, & \Sigma(\alpha^{(0)}) &= K(\sigma_{\delta, 0}, \ell_0) + \sigma_{\varepsilon, 0}^2 I_n, & s &= 0, 1, \\ \mathbf{p}_s^{(1)} &= \{p_s^{(1)}(t_i)\}_{i=1}^n, & \hat{\mathbf{p}}_s^{(1)}(\boldsymbol{\theta}) &= \{\hat{p}_s^{(1)}(t_i; \boldsymbol{\theta})\}_{i=1}^n, & \Sigma(\alpha^{(1)}) &= K(\sigma_{\delta, 1}, \ell_1) + \sigma_{\varepsilon, 1}^2 I_n, & s &= 1, 2, \end{aligned}$$

and assuming that our data set, say  $D$ , consists of four independent discrete time series,

$$D = \{D^{(0)}, D^{(1)}\} \in \mathbb{R}^{4n}, \quad D^{(0)} = \{\mathbf{p}_0^{(0)}, \mathbf{p}_1^{(0)}\} \in \mathbb{R}^{2n}, \quad D^{(1)} = \{\mathbf{p}_1^{(1)}, \mathbf{p}_2^{(1)}\} \in \mathbb{R}^{2n},$$

we arrive at the likelihood,

$$\Pr(D|\boldsymbol{\theta}, \alpha) = \Pr(D^{(0)}|\boldsymbol{\theta}, \alpha^{(0)}) \Pr(D^{(1)}|\boldsymbol{\theta}, \alpha^{(1)}), \quad (10)$$

where

$$\begin{aligned} \Pr(D^{(0)}|\boldsymbol{\theta}, \alpha^{(0)}) &= (2\pi)^{-n} |\Sigma(\alpha^{(0)})|^{-1} \prod_{s=0}^1 \exp\left(-\frac{1}{2}(\mathbf{p}_s^{(0)} - \mathbf{p}_s^{(0)}(\boldsymbol{\theta}))^\top \Sigma^{-1}(\alpha^{(0)}) (\mathbf{p}_s^{(0)} - \mathbf{p}_s^{(0)}(\boldsymbol{\theta}))\right), \\ \Pr(D^{(1)}|\boldsymbol{\theta}, \alpha^{(1)}) &= (2\pi)^{-n} |\Sigma(\alpha^{(1)})|^{-1} \prod_{s=1}^2 \exp\left(-\frac{1}{2}(\mathbf{p}_s^{(1)} - \mathbf{p}_s^{(1)}(\boldsymbol{\theta}))^\top \Sigma^{-1}(\alpha^{(1)}) (\mathbf{p}_s^{(1)} - \mathbf{p}_s^{(1)}(\boldsymbol{\theta}))\right). \end{aligned}$$

As prior for  $\boldsymbol{\theta}$ , we use a multivariate uniform distribution based on the deterministic characterization performed in [15]. Specifically, we set

$$\Pr(\boldsymbol{\theta}) = \prod_{i=1}^5 \Pr(\theta_i), \quad \theta_i \sim \text{Uniform}(l_i, u_i), \quad (11)$$

with

$$\begin{aligned} l_1/2\pi &= \bar{\omega}_{0,1}/2\pi - 10^{-3} \text{ GHz}, & u_1/2\pi &= \bar{\omega}_{0,1}/2\pi + 10^{-3} \text{ GHz}, & \bar{\omega}_{0,1}/2\pi &= 3.448646 \text{ GHz}, \\ l_2/2\pi &= \bar{\omega}_{1,2}^-/2\pi - 10^{-3} \text{ GHz}, & u_2/2\pi &= \bar{\omega}_{1,2}^-/2\pi + 10^{-3} \text{ GHz}, & \bar{\omega}_{1,2}^-/2\pi &= 3.240105 \text{ GHz}, \\ l_3/2\pi &= \bar{\omega}_{1,2}^+/2\pi - 10^{-3} \text{ GHz}, & u_3/2\pi &= \bar{\omega}_{1,2}^+/2\pi + 10^{-3} \text{ GHz}, & \bar{\omega}_{1,2}^+/2\pi &= 3.240403 \text{ GHz}, \end{aligned}$$

$$\begin{aligned} l_4 &= \bar{T}_{2,1} - 5 \mu\text{s}, & u_4 &= \bar{T}_{2,1} + 5 \mu\text{s}, & \bar{T}_{2,1} &= 13.07 \mu\text{s}, \\ l_5 &= \bar{T}_{2,2} - 1.5 \mu\text{s}, & u_5 &= \bar{T}_{2,2} + 1.5 \mu\text{s}, & \bar{T}_{2,2} &= 2.73 \mu\text{s}. \end{aligned}$$

We also use uniform priors for the hyper-parameters,

$$\Pr(\boldsymbol{\alpha}^{(0)}) = \Pr(\boldsymbol{\alpha}^{(1)}) = \prod_{i=1}^3 \Pr(\alpha_i), \quad \alpha_1, \alpha_2 \sim \text{Uniform}(1, 10^4), \quad \alpha_3 \sim \text{Uniform}(0.1, 10), \quad (12)$$

ensuring that they will remain positive while allowing them to take on large values.

With the full likelihood (10) and the priors (11)-(12) in hand, we can apply the proposed sampling methods of Sections 3 and 4 and Algorithm 1 to perform inference and prediction.

## 5.4 Results and discussions

We now present the results of the Bayesian quantum characterization with and without model discrepancy. Specifically, we consider three cases:

1. Characterization without model discrepancy;
2. Characterization including model discrepancy with a squared exponential covariance kernel ( $\gamma = 2$ );
3. Characterization including model discrepancy with an exponential covariance kernel ( $\gamma = 1$ ).

In all three cases, we run Algorithm 1 for  $M = 2 \times 10^4$  iterations and remove the first half of the samples, known as the burn-in period. We also use a thinning period of 2, that is, we discard every other sample in the chain to reduce the correlation between consecutive samples. As a result, we get a total of 5000 Markov chain samples for the parameters of interest. We use the symmetric proposals in (5) with the supports  $\mathbf{r}_\theta = (2\pi \times 10^{-6}, 2\pi \times 10^{-6}, 2\pi \times 10^{-6}, 0.2, 0.1)$  and  $\mathbf{r}_{\boldsymbol{\alpha}^{(0)}} = \mathbf{r}_{\boldsymbol{\alpha}^{(1)}} = (8, 8, 0.05)$ . As a standard test, for each approach, we run multiple Markov chains with different initial values of parameters and monitor the trace plots to ensure a good mixing and convergence of the chains and acceptance rates of 20 – 25%. The computational details specific to each case are given below.

### 5.4.1 Approach 1: characterization without model discrepancy

This example is similar to the example presented in [15], with three main differences: 1) while the authors in [15] consider only the three transition frequencies as main parameters in the Bayesian inference, here we also include the two pure dephasing time scales in the parameter vector  $\boldsymbol{\theta}$ . 2) Instead of imposing informative priors on the hyper-parameters, as done in [15], we avoid making strong *a priori* assumptions by only imposing flat priors on the hyper-parameters. 3) we consider dark times up to 10  $\mu\text{s}$ , which is twice as long as the dark times considered in [15]. We use Algorithm 1 with the likelihood function (10), but exclude the Gaussian process covariance matrix  $K$  from the covariance matrix  $\Sigma$ . That is, we consider the covariance only due to experimental noise:  $\Sigma(\boldsymbol{\alpha}^{(k)}) = \sigma_{\varepsilon,k}^2 I_n$ , with  $k = 0, 1$ .

The posterior densities and the mean and standard deviation of the five main parameters  $\boldsymbol{\theta}$  can be found in Figure 2 and Table 1, respectively. The posterior densities are obtained by normalizing their corresponding histograms generated by the Markov chain samples. The mean of hyper-parameters, i.e., the standard deviations  $(\sigma_{\varepsilon,0}, \sigma_{\varepsilon,1})$  of the experimental noise are given in Table 2. We also overlay 500 simulations of Lindblad's master equation on top of the experimental measurements, where each simulation corresponds to a sample from the Markov chains of Lindblad's parameters; see the top panels in Figure 3 and Figure 4. We observe that while the predicted simulations follow the measurement trajectories on average, they fail to capture the uncertainty present in the measurements. In other words,

although the uncertain model predictions are rather consistent in the mean with the measurements, their degree of uncertainty is inconsistent with the discrepancy from the measurements. This is also apparent from the very small noise variances (see the second column of Table 2). There may be two reasons for this failure. One reason is that a Gaussian likelihood model that is built upon the assumption that the noise is independently and identically distributed may not be capable of representing the complex noise structure of Ramsey measurements. A second reason, that is the subject of our focus here, is due to the inadequacy of Lindblad’s model in describing the quantum system. As reported in [26], not accounting for model discrepancy may lead to “overconfident” parameter estimates that in turn produce predictions with misleadingly small error ranges.

#### 5.4.2 Approach 2: characterization including model discrepancy with a squared exponential covariance kernel

We next consider a discrepancy model, added externally to the simulation model as in (7)-(8), and given by a Gaussian process with the squared exponential covariance kernel (9) with  $\gamma = 2$ . Since we have analytical formulas for the eigenpairs of squared-exponential covariance kernels, we opt for the method of Section 3 to evaluate the likelihood function (10) in a numerically stable and efficient way. Retaining only  $r = 5$  eigen-modes (out of  $n = 500$ ) in the eigen-expansion of each covariance kernel, when a Gaussian measure  $\mu$  with standard deviation  $\sigma = 0.01$  is used, enables us to approximate the covariance matrices with relative errors smaller than  $10^{-2}$  in Frobenius norm.

The posterior densities and the mean and standard deviation of the five main parameters  $\theta$  can be found in Figure 2 and Table 1, respectively. The mean of hyper-parameters, i.e., the standard deviations of experimental noise and the covariance kernel parameters, are given in Table 2. We also overlay 500 realizations of the predictive Gaussian process overlaid on top of the experimental measurements, see the middle panels in Figure 3 and Figure 4. Each realization of the Gaussian process is drawn from the predictive conditional distribution, as explained in Section 2.3. The predicted realizations show better qualitative agreement and consistency with experimental measurements, compared to the previous case where model discrepancy is ignored.

#### 5.4.3 Approach 3: characterization including model discrepancy with an exponential covariance kernel

Finally, we consider a discrepancy model similar to the previous case, but with an exponential covariance kernel (9) with  $\gamma = 1$ . That is, we consider a less smooth covariance structure compared to the previous case. In the absence of analytical formulas for the eigenpairs of exponential covariance kernels, we utilize the method of Section 4, retaining the  $r = 25$  largest eigenvalues (and corresponding eigenvectors) of the covariance matrix, and marginalize over the remaining  $n - r = 475$  modes.

The posterior densities and the mean and standard deviation of the five main parameters  $\theta$  can be found in Figure 2 and Table 1, respectively. The mean of the hyper-parameters are given in Table 2. We also overlay 500 realizations of the predictive Gaussian process overlaid on top of the experimental measurements, see the bottom panels in Figure 3 and Figure 4. The predicted realizations show a higher consistency with experimental measurements and the degree of uncertainty in the measurements, in particular compared to the case without the model discrepancy. The improvements over the case with the squared exponential covariance model are less pronounced, but still noticeable. This suggests that including model discrepancy is important, and that the smoothness of the covariance kernel representation of the model discrepancy (e.g. induced by the parameter  $\gamma$  in the covariance kernel) also matters for making reliable and consistent predictions.



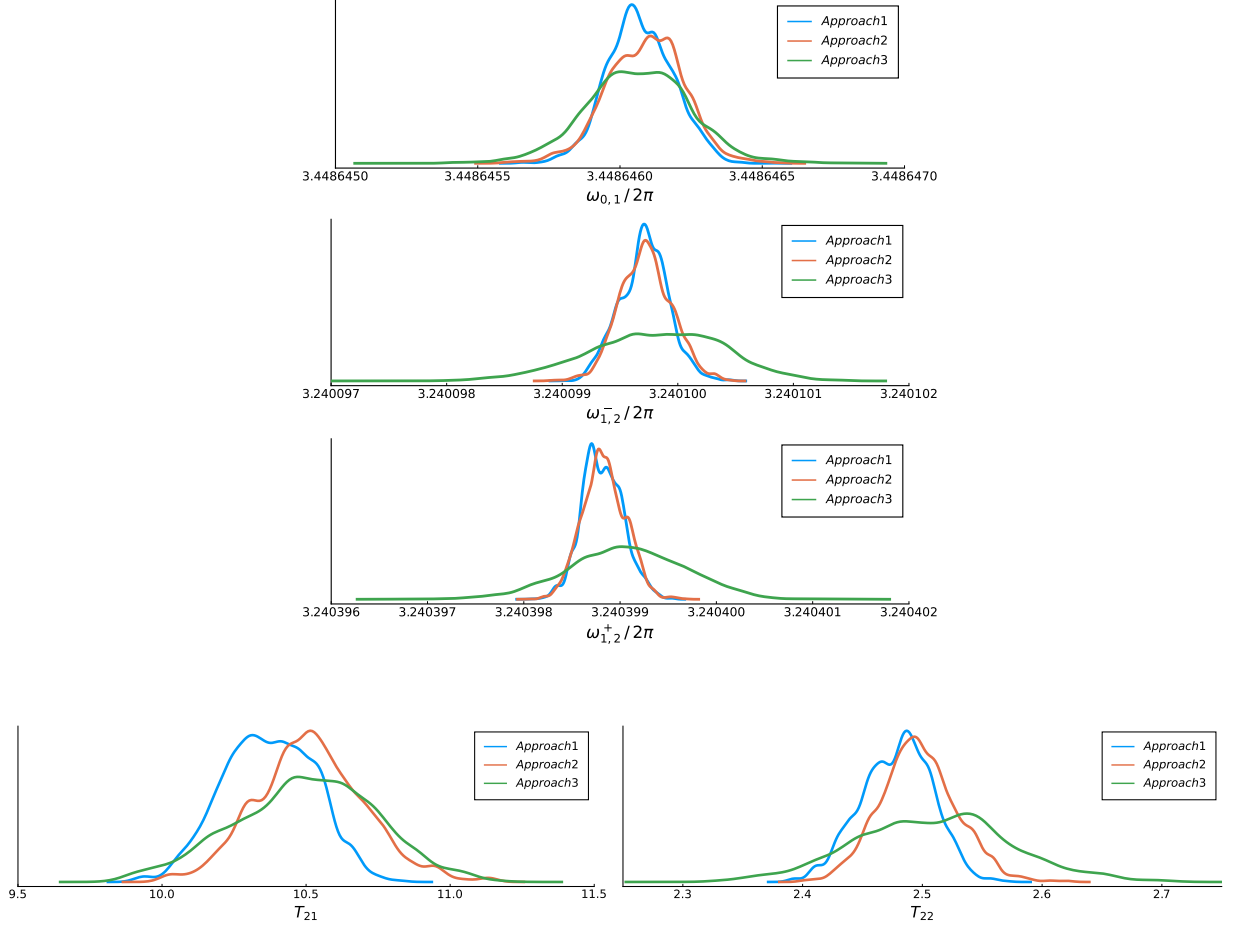


Figure 2: Posterior densities of the main five parameters  $\theta$  (transition frequencies and dephasing times) approximated by normalizing the Markov chain samples obtained by the three approaches, with and without the Gaussian process (GP). Here, approach # 1 excludes the GP, #2 uses a GP with a squared-exponential covariance kernel, and # 3 uses a GP with an exponential covariance kernel.

Parameters	Mean			Standard Deviation		
	no GP	GP/w SEK	GP/w EK	no GP	GP/w SEK	GP/w EK
$\omega_{01}/2\pi$	3.448 646 GHz	3.448 646 GHz	3.448 646 GHz	0.11 kHz	0.13 kHz	0.19 kHz
$\omega_{12}^-/2\pi$	3.240 100 GHz	3.240 100 GHz	3.240 100 GHz	0.21 kHz	0.23 kHz	0.56 kHz
$\omega_{12}^+/2\pi$	3.240 399 GHz	3.240 399 GHz	3.240 399 GHz	0.21 kHz	0.23 kHz	0.59 kHz
$T_{2,1}$	10.43 $\mu s$	10.44 $\mu s$	10.50 $\mu s$	0.136 $\mu s$	0.183 $\mu s$	0.251 $\mu s$
$T_{2,2}$	2.48 $\mu s$	2.49 $\mu s$	2.51 $\mu s$	0.027 $\mu s$	0.031 $\mu s$	0.064 $\mu s$

Table 1: Statistical summaries, including mean and standard deviation of transition frequencies and dephasing times determined by the three Bayesian characterization approaches. Here, GP stands for Gaussian process, SEK is the squared exponential covariance kernel, and EK is the exponential covariance kernel.

Hyper-parameters	Mean		
	no GP	GP/w SEK	GP/w EK
$\sigma_{\varepsilon,0}$	0.0319	0.0382	0.0531
$\sigma_{\delta,0}$	—	0.0568	0.0406
$\ell_0$	—	1.9849	2.5219
$\sigma_{\varepsilon,1}$	0.0274	0.0292	0.0725
$\sigma_{\delta,1}$	—	0.0394	0.0526
$\ell_1$	—	1.7263	2.0494

Table 2: Mean of hyper-parameters by the three Bayesian characterization approaches: no Gaussian process (GP), a GP with the squarred-exponential covariance kernel (SEK), and a GP with the exponential covariance kernel (EK).

## 6 Conclusions

The conventional Bayesian quantum characterization approaches often only consider experimental uncertainty and neglect uncertainties in the dynamical model. Consequently, they may lead to model predictions that are inconsistent with quantum measurements. In this paper, we have developed a Bayesian approach that accounts for model uncertainty, represented by a Gaussian process that is added to a Lindbladian dynamical model. Focusing on data from Ramsey measurements obtained from the QuDIT system at Lawrence Livermore National Laboratory, we have demonstrated that the proposed method produces predictive uncertainties that are consistent with the uncertainty in the data. We have also exemplified that ignoring model uncertainty leads to predictions that fail to capture the full range of uncertainties in the data.

In the current study, we have considered an explicit representation of modeling uncertainty by adding an external model discrepancy term (being a Gaussian process) to the simulated data. This may, however, cause two difficulties. First, it may violate physical laws: the resulting model may, for example, predict populations below zero, or above one. Secondly, in some cases it may fail to improve the predictive capability of the model because it is only trained on data from a specific type of experiment. Indeed, the approach considered here only provides a model discrepancy correction for the quantity that is being measured within a Ramsey experiment. Therefore, the model is not directly applicable for predicting other quantities, or across different experimental scenarios. To mitigate these shortcomings, future research on quantum characterization should consider internal representations of model discrepancy, for example by embedding the discrepancy within the simulation model. This would, for example, allow model discrepancy to be deployed when solving quantum optimal control problems using risk-neutral methodologies, potentially leading to control pulses with improved resilience to noise.

## Acknowledgements

The authors gratefully acknowledge support from the U.S. Department of Energy, Office of Advanced Scientific Computing Research, through the Advanced Research in Quantum Computing program, project TEAM, award SCW-1683.1. The authors are also grateful to Dr. Gabriel Huerta at Sandia National Laboratory for his guidance and stimulating discussions. We also thank Dr. Yujin Cho for her help in explaining experimental intricacies of the QuDIT device at Lawrence Livermore National Laboratory. This work was performed under the auspices of the U.S. Department of Energy by Lawrence Livermore National Laboratory under Contract DE-AC52-07NA27344. This is contribution LLNL-JRNL-853217.

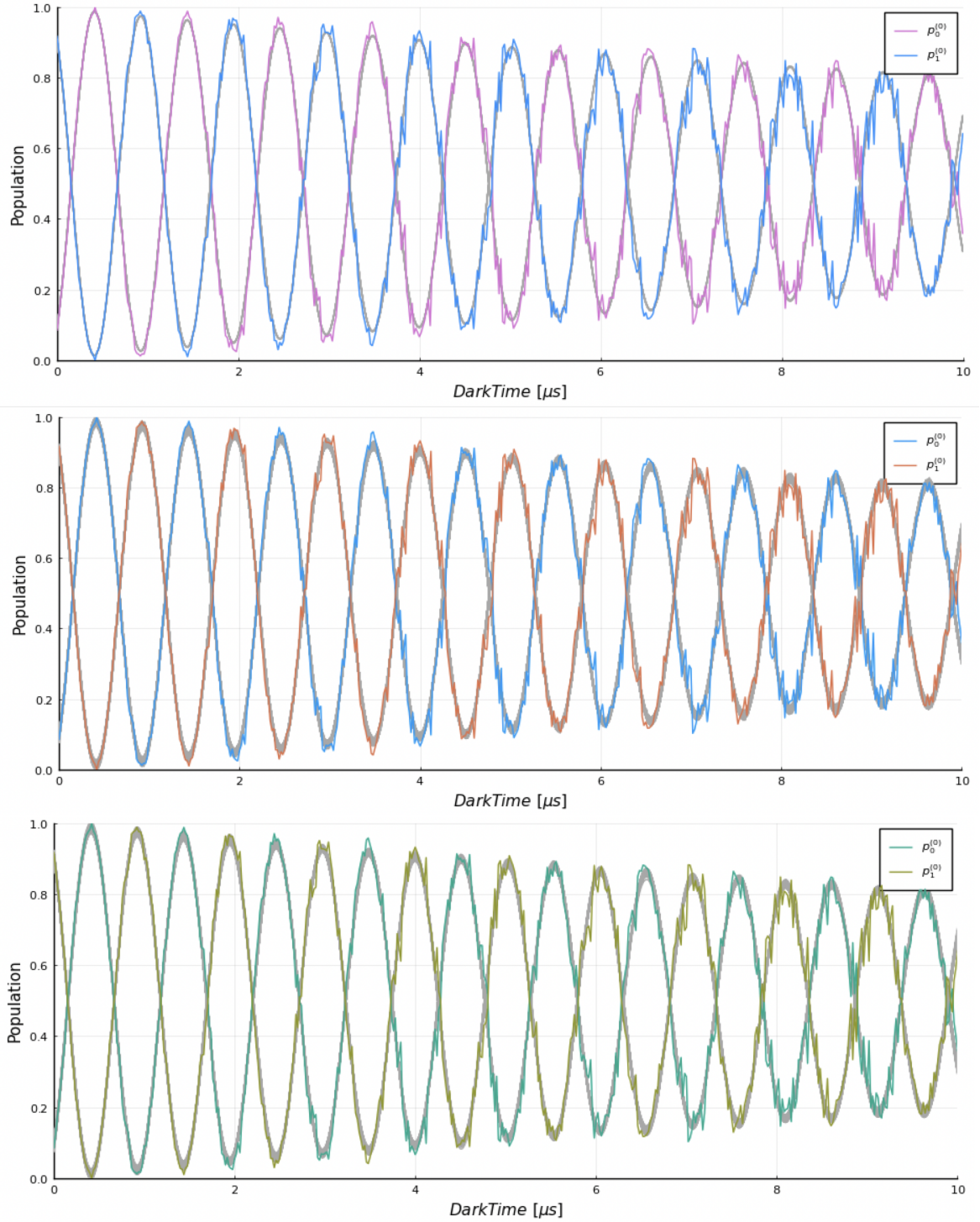


Figure 3: Comparison between Ramsey  $0 \leftrightarrow 1$  experimental measurements (colored lines) and 500 realizations drawn from the predictive distributions (gray lines), obtained by the Bayesian analysis that excludes model discrepancy (top) and includes model discrepancy using a squared exponential covariance kernel (middle) and an exponential covariance kernel (bottom). The variable thickness of the gray lines in the middle and bottom panels is a result of including uncertainties from both measurement and model prediction.

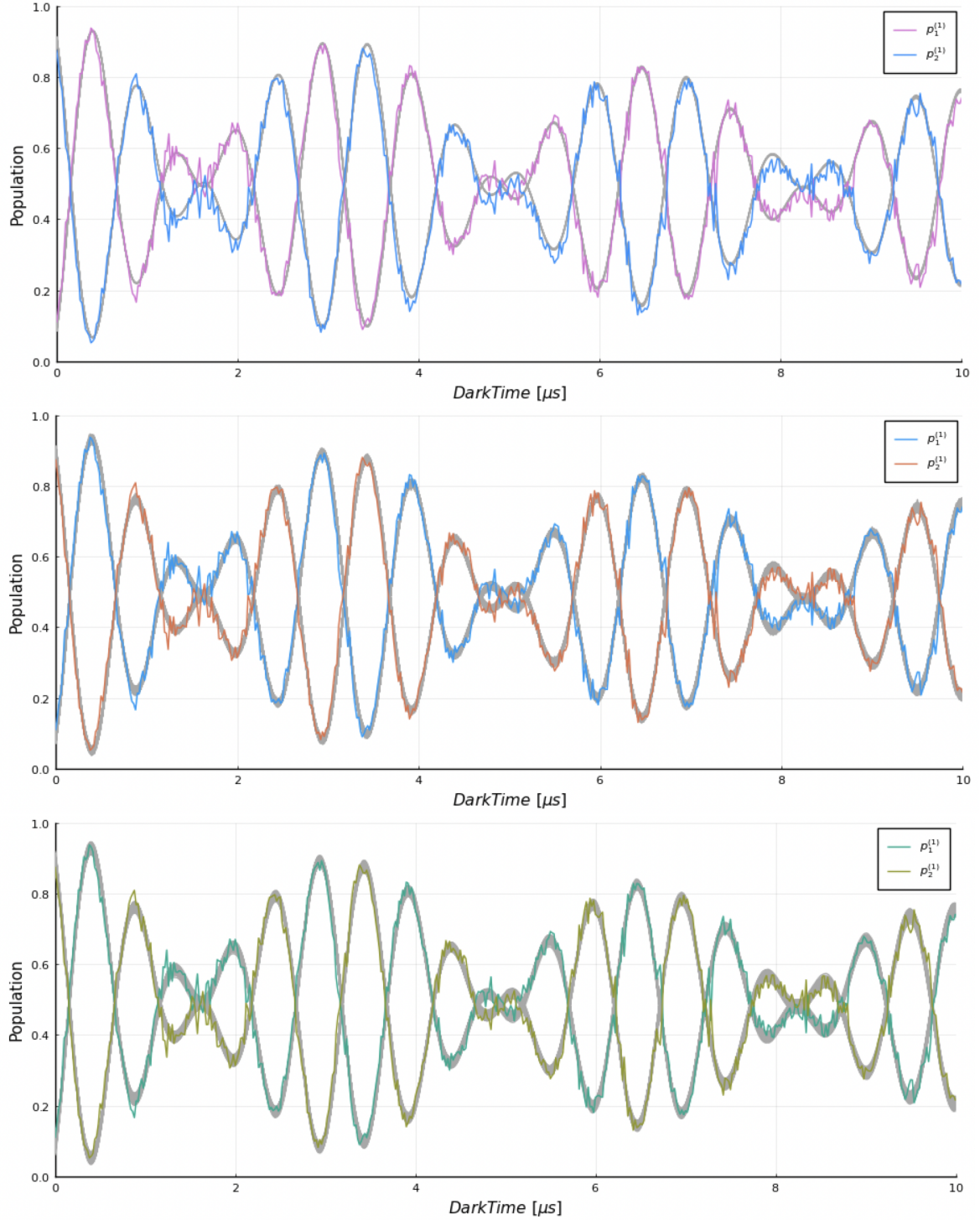


Figure 4: Comparison between Ramsey  $1 \leftrightarrow 2$  experimental measurements (colored lines) and 500 realizations drawn from the predictive distributions (gray lines), obtained by the Bayesian analysis that excludes model discrepancy (top) and includes model discrepancy using a squared exponential covariance kernel (middle) and an exponential covariance kernel (bottom). The variable thickness of the gray lines in the middle and bottom panels is a result of including uncertainties from both measurement and model prediction.

## References

- [1] S. J. Glaser, U. Boscain, T. Calarco, C. P. Koch, W. Köckenberger, R. Kosloff, I. Kuprov, B. Luy, S. Schirmer, T. Schulte-Herbrüggen, et al. Training Schrödinger’s cat: Quantum optimal control: Strategic report on current status, visions and goals for research in Europe. *The European Physical Journal D*, 69:1–24, 2015.
- [2] C. P. Koch, U. Boscain, T. Calarco, G. Dirr, S. Filipp, S. J. Glaser, R. Kosloff, S. Montangero, T. Schulte-Herbrüggen, D. Sugny, et al. Quantum optimal control in quantum technologies. Strategic report on current status, visions and goals for research in Europe. *EPJ Quantum Technology*, 9:19, 2022.
- [3] M. J. Peterer, S. J. Bader, X. Jin, F. Yan, A. Kamal, T. J. Gudmundsen, P. J. Leek, T. P. Orlando, W. D. Oliver, and S. Gustavsson. Coherence and decay of higher energy levels of a superconducting transmon qubit. *Physical review letters*, 114:010501, 2015.
- [4] P. Krantz, M. Kjaergaard, F. Yan, T. P. Orlando, S. Gustavsson, and W. D. Oliver. A quantum engineer’s guide to superconducting qubits. *Applied physics reviews*, 6:021318, 2019.
- [5] N. Wittler, F., Roy, K. Pack, M. Werninghaus, A. S. Roy, D. J. Egger, S. Filipp, F. K. Wilhelm, and S. Machnes. Integrated tool set for control, calibration, and characterization of quantum devices applied to superconducting qubits. *Physical Review Applied*, 15:034080, 2021.
- [6] K. Bharti, A. Cervera-Lierta, T. H. Kyaw, T. Haug, S. Alperin-Lea, A. Anand, M. Degroote, H. Heimonen, J. S. Kottmann, T. Menke, et al. Noisy intermediate-scale quantum algorithms. *Reviews of Modern Physics*, 94:015004, 2022.
- [7] N. Wiebe, C. Granade, C. Ferrie, and D. G. Cory. Hamiltonian learning and certification using quantum resources. *Phys. Rev. Lett.*, 112:190501, 2014.
- [8] N. Wiebe, C. Granade, C. Ferrie, and D. G. Cory. Quantum Hamiltonian learning using imperfect quantum resources. *Phys. Rev. A*, 89:042314, 2014.
- [9] N. Wiebe, C. Granade, and D. G. Cory. Quantum bootstrapping via compressed quantum Hamiltonian learning. *New Journal of Physics*, 17:022005, 2015.
- [10] J. Wang, S. Paesani, R. Santagati, S. Knauer, A. Gentile, N. Wiebe, M. Petruzzella, J. L. O’Brien, J. G. Rarity, A. Laing, et al. Experimental quantum Hamiltonian learning. *Nature Physics*, 13:551–555, 2017.
- [11] J. F. Ralph, S. Maskell, and K. Jacobs. Multiparameter estimation along quantum trajectories with sequential Monte Carlo methods. *Phys. Rev. A*, 96:052306, 2017.
- [12] T. J. Evans, R. Harper, and S. T. Flammia. Scalable Bayesian Hamiltonian learning. *arXiv:1912.07636*, 2023.
- [13] R. Bennink, A. Jasra, K. J. H. Law, and P. Lougovski. Estimation and uncertainty quantification for the uotput from quantum simulations. *Foundations of Data Science*, 1:157–176, 2019.
- [14] A. A. Gentile, B. Flynn, S. Knauer, N. Wiebe, S. Paesani, C. E. Granade, J. G. Rarity, R. Santagati, and A. Laing. Learning models of quantum systems from experiments. *Nature Physics*, 17:837–843, 2021.

- [15] Z. Peng, D. Appelö, N. A. Petersson, M. Motamed, F. Garcia, and Y. Cho. Deterministic and Bayesian characterization of quantum computing devices. *arXiv:2306.13747*, 2023.
- [16] A. Shapiro, D. Dentcheva, and A. Ruszczyński. *Lectures on stochastic programming: modeling and theory*. SIAM, 2021.
- [17] A. P. M. Place, L. V. H. Rodgers, P. Mundada, B. M. Smitham, M. Fitzpatrick, Z. Leng, A. Premkumar, J. Bryon, A. Vrajitoarea, S. Sussman, et al. New material platform for superconducting transmon qubits with coherence times exceeding 0.3 milliseconds. *Nature communications*, 12(1):1–6, 2021.
- [18] G. Lindblad. On the generators of quantum dynamical semigroups. *Communications in Mathematical Physics*, 48:119–130, 1976.
- [19] D. Tupkary, A. Dhar, M. Kulkarni, and A. Purkayastha. Fundamental limitations in Lindblad descriptions of systems weakly coupled to baths. *Phys. Rev. A*, 105:032208, 2022.
- [20] M. C. Kennedy and A. O’Hagan. Bayesian calibration of computer models. *Journal of the Royal Statistical Society: Series B (Statistical Methodology)*, 63:425–464, 2001.
- [21] M. Goldstein and J. Rougier. Probabilistic formulations for transferring inferences from mathematical models to physical systems. *SIAM J. Sci. Comput.*, 26:467–487, 2004.
- [22] D. Higdon, M. Kennedy, J. C. Cavendish, J. A. Cafeo, and R. D. Ryne. Combining field data and computer simulations for calibration and prediction. *SIAM J. Sci. Comput.*, 26:448–466, 2004.
- [23] M. J. Bayarri, J. O. Berger, R. Paulo, J. Sacks, J. A. Cafeo, J. Cavendish, C.-H. Lin, and J. Tu. A framework for validation of computer models. *Technometrics*, 49:138–154, 2007.
- [24] D. Higdon, J. Gattiker, B. Williams, and M. Rightley. Computer model calibration using high-dimensional output. *Journal of the American Statistical Association*, 103:570–583, 2008.
- [25] G. Han, T. J. Santner, and J. J. Rawlinson. Simultaneous determination of tuning and calibration parameters for computer experiments. *Technometrics*, 51:464–474, 2009.
- [26] J. Brynjarsdottir and A. O’Hagan. Learning about physical parameters: the importance of model discrepancy. *Inverse Problems*, 30:114007, 2014.
- [27] Y. Ling, J. Mullins, and S. Mahadevan. Selection of model discrepancy priors in bayesian calibration. *Journal of Computational Physics*, 276:665–680, 2014.
- [28] S. Sankararaman and S. Mahadevan. Integration of model verification, validation, and calibration for uncertainty quantification in engineering systems. *Reliability Engineering and System Safety*, 138:194–209, 2015.
- [29] K. A. Maupin and L. P. Swiler. Model discrepancy calibration across experimental settings. *Reliability Engineering and System Safety*, 200:106818, 2020.
- [30] K. Sargsyan, H. N. Najm, and R. Ghanem. On the statistical calibration of physical models. *International Journal of Chemical Kinetics*, 47:246–276, 2015.
- [31] T. Portone, D. McDougall, and R. D. Moser. A stochastic operator approach to model inadequacy with applications to contaminant transport. *arXiv:1702.07779*, 2017.

- [32] R. Morrison, T. Oliver, and R. Moser. Representing model inadequacy: A stochastic operator approach. *SIAM J. Uncertainty Quantification*, 6:457–496, 2018.
- [33] K. Sargsyan, X. Huan, and H. N. Najm. Embedded model error representation for Bayesian model calibration. *Int. J. Uncertainty Quantification*, 9:365–394, 2019.
- [34] A. Gelman, J. B. Carlin, H. S. Stern, and D. B. Rubin. *Bayesian data analysis*. Chapman and Hall/CRC, 2004.
- [35] T. Bayes, R. Price, and J. Canton. An essay towards solving a problem in the doctrine of chances. By the late Rev. Mr. Bayes, F. R. S. communicated by Mr. Price, in a letter to John Canton, A. M. F. R. *Philosophical Transactions of the Royal Society of London*, pages 370–418, 1763.
- [36] C. E. Rasmussen and C. K. I. Williams. *Gaussian Processes for Machine Learning*. The MIT Press, 2006.
- [37] T. Shi, M. Belkin, and B. Yu. Data spectroscopy: Eigenspaces of convolution operators and clustering. *Ann. Statist.*, 37:3960–3984, 2009.
- [38] L. Guttman. Enlargement methods for computing the inverse matrix. *Ann. Math. Statist.*, 17:336–343, 1946.
- [39] P.-G. Martinsson and J. A. Tropp. Randomized numerical linear algebra: Foundations and algorithms. *Acta Numerica*, 29:403–572, 2020.
- [40] E. J. Nyström. Über die praktische auflösung von integralgleichungen mit anwendungen auf randwertaufgaben. *Acta Mathematica*, 54:185–204, 2021.
- [41] D. G. Tempel and A. Aspuru-Guzik. Relaxation and dephasing in open quantum systems time-dependent density functional theory: Properties of exact functionals from an exactly-solvable model system. *Chemical Physics*, 391:130–142, 2011.
- [42] IBM-Quantum. Qiskit: Calibrating qubits with Qiskit Pulse. <https://learn.qiskit.org/v1/course/quantum-hardware-pulses/calibrating-qubits-pulse>.
- [43] D. Ristè, C. C. Bultink, M. J. Tiggelman, R. N. Schouten, K. W. Lehnert, and L. DiCarlo. Millisecond charge-parity fluctuations and induced decoherence in a superconducting transmon qubit. *Nature communications*, 4:1–6, 2013.
- [44] D. M. Tennant, L. A. Martinez, K. M. Beck, S. R. O’Kelley, C. D. Wilen, R. McDermott, J. L. DuBois, and Y. J. Rosen. Low-frequency correlated charge-noise measurements across multiple energy transitions in a tantalum transmon. *PRX Quantum*, 3:030307, 2022.
- [45] M. Nielsen and I. Chuang. *Quantum computation and quantum information*. Cambridge University Press, 2000.
- [46] Z. Peng, D. Appelö, N. A. Petersson, F. Garcia, and Y. Cho. Mathematical approaches for characterization, control, calibration and validation of a quantum computing device. *arXiv preprint arXiv:2301.10712*, 2023.
- [47] N. A. Petersson, F. M. Garcia, D. E. A. Appelö, S. Günther, Y. Choi, and R. Vogt. Quantum Physics without the Physics. *arXiv preprint arXiv:2012.03865*, 2020.